Math Geosci (2008) 40: 249–275
DOI 10.1007/s11004-008-9149-5

Kinematics-Based Mathematical Model for Deforming Thrust Wedges

Matty Mookerjee · Gautam Mitra

Received: 22 December 2006 / Accepted: 23 January 2008 / Published online: 11 March 2008

Abstract Given the wealth of data concerning the kinematics of deforming fold-thrust belts (FTBs), first-order generalizations about how the major strain components vary within a deforming thrust wedges are considered. These generally observed strain patterns are used to constrain a general, kinematics-based, FTB-wedge model. We considered five strain components within a deforming thrust sheet: (1) thrust-parallel simple shear, (2) horizontal contractional strain, (3) thrust-normal reaction strain, (4) gravitational strain, and (5) a lateral confining boundary condition. After making assumptions about how these strain components vary within a model FTB-wedge, the incremental deformation matrix can be calculated for any given point within the deforming wedge. Thus, the material path of a given marker can be determined and an initially spherical marker's strain path can be calculated as it moves through the deforming wedge. Furthermore, by illustrating various kinematic parameters of many initially spherical markers (for example, Flinn's k-value, incremental octahedral shear strain, transport-perpendicular stretch), we have assembled representations of the kinematic properties of the entire model wedge. By including a flat-ramp-flat fault surface geometry for the model wedge, we are able to examine the kinematic effects of this relatively common structural geometry. Within the fault ramp segment there are greater incremental strain magnitudes, out-of-the-plane motion, and flattening strains. Additionally, data from this model suggests that gravitational strains potentially have a significant effect on the strain distribution within a deforming thrust wedge.

M. Mookerjee is formerly Matthew Strine.

M. Mookerjee (✉)
Department of Geology, Sonoma State University, Rohnert Park, CA 94928, USA
e-mail: matty.mookerjee@sonoma.edu

G. Mitra
Department of Earth and Environmental Sciences, University of Rochester, Rochester, NY 14627, USA

Keywords Thrust sheets · Kinematics · Strain · Deformation · Shear zone · Thrust fault

1 Introduction

Mechanical and numerical models have been responsible for considerable advancements in the understanding of the structural evolution of mountain-belts, particularly within fold-thrust belts (FTB) (Chapple 1978; Davis et al. 1983; Erickson and Jamison 1995; Strayer and Suppe 2002; Kwon and Mitra 2004). It is important to recognize that all models have their limitations, mostly associated with the assumptions incorporated. Most mechanical models make assumptions about forces and boundary conditions. An alternative approach is to make assumptions about how various components of strain are distributed throughout the deforming FTB-wedge. The benefit of the latter is that detailed strain and particle paths are easily determined as are the incremental strain distributions. Additionally, our assumptions are based on well-documented field data as opposed to stress fields which are exceedingly difficult to determine. Since our assumptions are based on the distribution of deformation components and displacements, we consider our model to be a kinematics-based as opposed to a mechanical-based mathematical model.

Using field-based observations, we make generalizations about strain patterns within naturally deformed FTB-wedges. These generalizations are then used to constrain our kinematics-based numerical model. The model takes into account five separate strain components: (1) thrust-parallel simple shear, (2) horizontal, motion plane-parallel, uniaxial shortening (contractional strain), (3) thrust-normal, uniaxial shortening (reaction strain), (4) vertical, uniaxial shortening (gravitational strain), and (5) horizontal, motion plane-normal, uniaxial shortening (a lateral confining boundary condition) (Fig. 1). These strain components vary independently within the wedge depending on the dip of the fault, the horizontal position within the wedge, the depth, and the normal distance away from the fault surface. As initially spherical markers move through the wedge, they will experience different incremental strains at each position within the wedge, the sum of which has the potential for yielding relatively complex strain paths. The addition of a flat–ramp–flat fault geometry compounds the complexity of the strain path while giving insight into the kinematics of a common

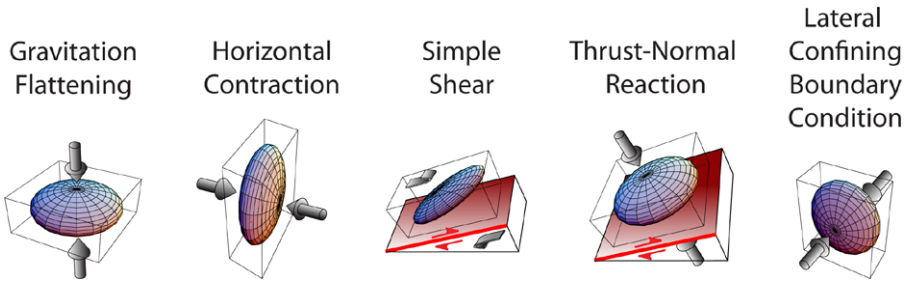

Fig. 1 The five strain components in our numerical model: gravitational strain (ε_g), horizontal contraction strain (ε_{tc}), simple shear strain (ε_{ss}), thrust normal reaction strain, (ε_{rnx}), and lateral confining strain (ε_{bc})

structural geometry. The model has shown that the deformation within the ramp segment of a deforming wedge has larger incremental strain magnitudes that are dominated by flattening strains when compared to the adjacent thrust flats. Also, note that the vertical gravitational strain component may have a considerable effect on the strain distribution within a deforming FTB wedge; in particular, this strain has a large effect on the incremental, out-of-the-plane motion within the wedge.

2 Mathematical Model Set-up and Design

2.1 Overview

The general approach taken in constructing the numerical model is to set up an initially straight line of spherical markers, that we will call observation markers. These can be tracked as they move through the deforming wedge. The initially straight line of observation markers is oriented perpendicular to the thrust surface. Deformation is split into a component of thrust parallel, basal-displacement followed by a component of pure strain (distortion of the initially spherical observation markers). In addition to determining the incremental strain, the incremental deformation matrices are used to determine the material displacement of the observation markers. While it is a simplification to consider basal-displacement and strain to be taking place as two distinct increments, the effect of this simplification is minimized by running the model with many closely spaced increments of deformation. The more increments of deformation, the more closely the model approximates simultaneous pure strain and thrust-parallel displacement. At the outset, the model assumes relationships for the manner in which five strain components vary throughout the wedge (discussed later). Therefore, at any point within the wedge, an incremental deformation matrix can be assembled (Fossen and Tikoff 1993; Tikoff and Fossen 1993; Jiang and Williams 1998; Lin et al. 1998). This is done for each of the observation markers for each increment of deformation. In this way, detailed strain path information for each of the observation markers can be determined. Since the line of observation markers moves through the wedge, generalizations concerning the kinematics and strain patterns of the entire deforming wedge can be made.

2.2 Input Data

The first component of the numerical model is the "input data" which can be separated into three categories: model-run parameters, geometric input parameters, and geologic input parameters (Fig. 2). Model-run parameters are simply logistical inputs concerning a given run which include the number of increments of deformation, the number of observation markers, and the level of precision for our "find root" function. Geometric input includes all parameters that will ultimately determine the geometry of the deforming wedge. These include parameters such as the dip of the fault along the flats (β), the dip of the fault on the ramp segment (Γ), the surface slope of the thrust wedge (α), the length of each of the fault segments, and the height of the rear of the wedge. The entire complement of geometric input

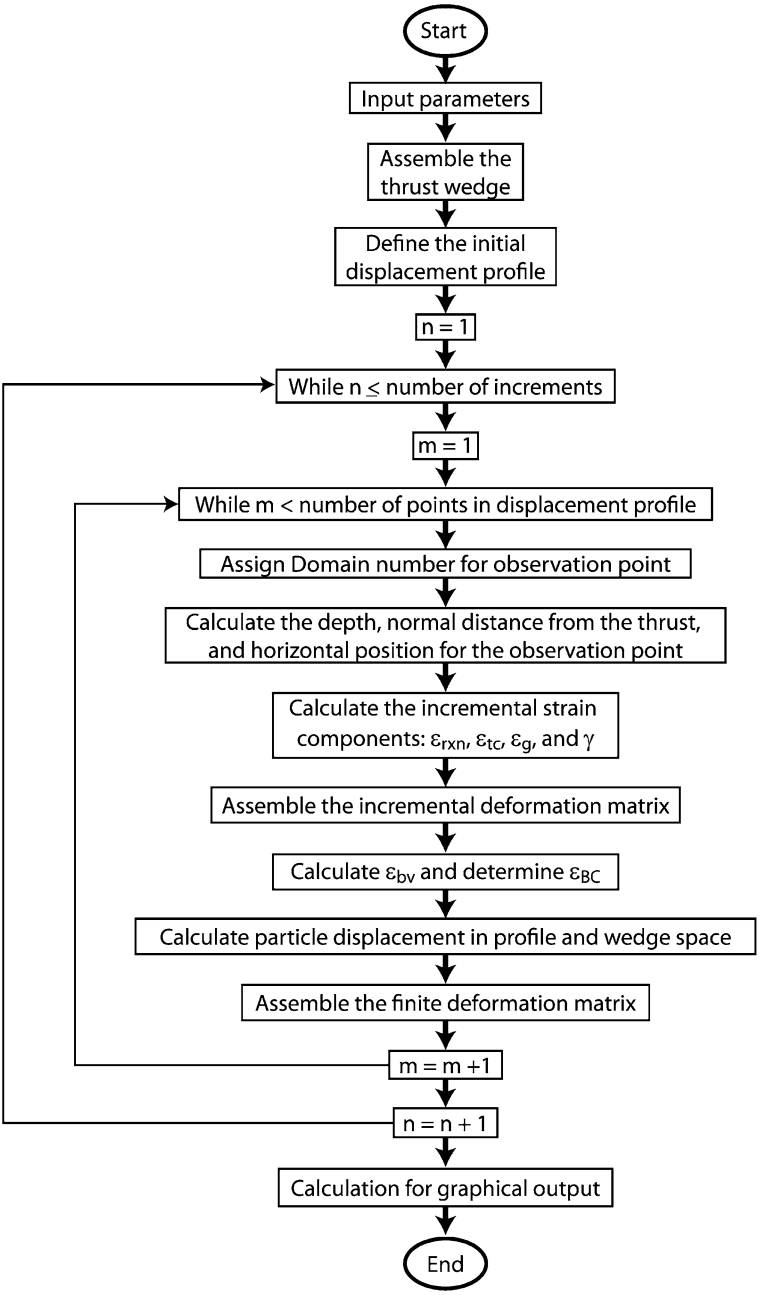

Fig. 2 A flow chart outlining the major components of our mathematical model program

parameters is illustrated in Fig. 3. For simplicity's sake the wedge is assumed to have already achieved a steady-state topography such that erosion is keeping pace with

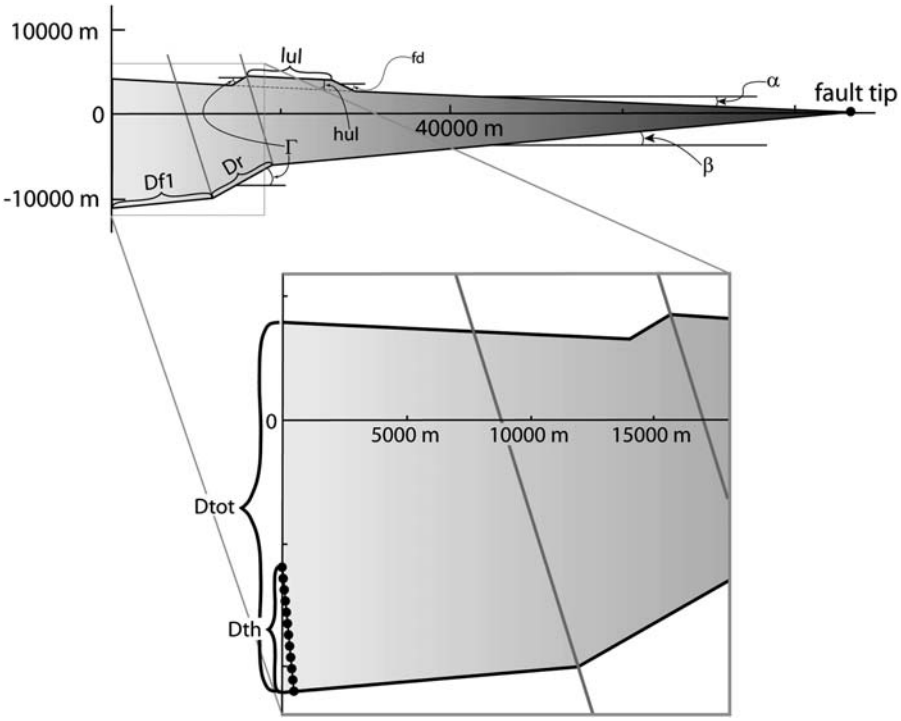

Fig. 3 The geometry of the deforming thrust wedge used within our numerical model. Dtot, Df1, Dr, Dth, Γ, α, β, fd, lul, and hul are all input data. All other wedge parameters are calculated from these data

uplift and the wedge remains a constant shape. Willet (1999) shows convincingly that topography in an FTB wedge will tend toward steady state because of the positive feedback between erosion rates and elevation. In detail, steady states in geologic settings are ephemeral at best, and a deforming thrust wedge will increase in length and decrease in taper throughout its deformation history (DeCelles and Mitra 1995; Mitra 1997). The output of this model incorporates a finite length of time which is shorter than the entire history of the deforming FTB-wedge and an amount of deformation that is less than the entire strain history for the wedge. In essence, we are only looking at an increment of deformation, albeit a relatively long increment. Also, included in the geometric input parameters is the vertical height of our line of observation markers (Dth) (Fig. 3). Since the bulk of the deformation within thrust wedges is confined to the areas adjacent to the thrust surface and because of the computational cost, we have restricted the height of Dth to five kilometers above the thrust surface.

Our last category of input data is geologic input. Incorporated into these data are many of our assumptions about how strain varies within a deforming wedge. For instance, we have assumed that simple shear deformation within the wedge is inhomogeneous and decreases exponentially with increased normal distance away from the thrust surface. It is a long-standing observation that deformation is heterogeneously distributed within natural shear zones, and that strain increases dra-

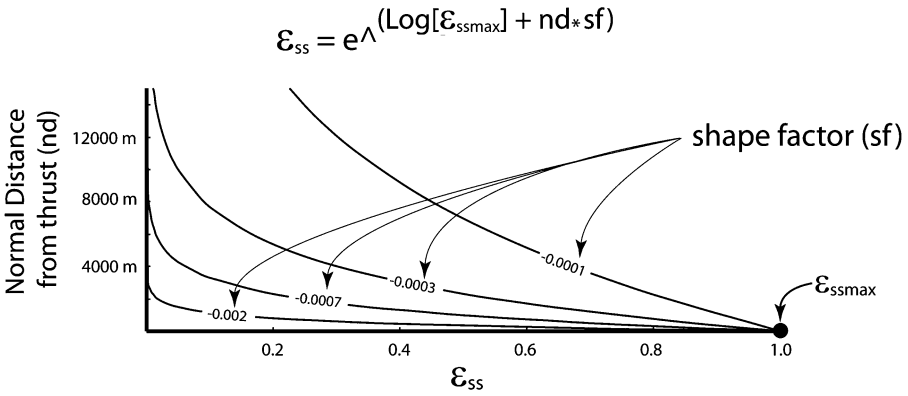

Fig. 4 The general form for the assumed relationship between simple shear strain, ε_{ss}, and the normal distance from the thrust surface, nd, for our numerical model. ε_{ssmax} determines the amount of simple shear exactly at the thrust surface, and the shape factor (sf) determines how rapidly the simple shear strain tapers off away from the thrust

matically within the middle of the zone and tapers off gradually towards the boundaries (Ramsay and Graham 1970; Mitra 1979; Ramsay and Huber 1983; Law 1987). For a thrust wedge, this type of heterogeneous strain pattern can be described mathematically using an exponential relationship of the form

$$\varepsilon_{ss} = e^{(\mathrm{Log}[\varepsilon_{ssmax}]+\mathrm{nd}\cdot\mathrm{sf})}, \tag{1}$$

where ε_{ss} is the thrust parallel simple shear strain, ε_{ssmax} is the strain immediately above the thrust surface, nd is the normal distance away from the thrust, and sf a shape factor that determines how rapidly the strain decreases away from the thrust (Fig. 4) (Table 1). Simple shear deformation is invariably related to the amount of friction along the thrust surface. In this numerical model, both ε_{ssmax} and sf are geologic input parameters. However, since we have no intuitive feel for appropriate values for sf, the amount of simple shear strain (octahedral shear strain) experienced at 1000 meters normal distance away from the thrust, ε_{ss1000} is inputted. Using ε_{ss1000}, ε_{ssmax} and (1), a value for sf is calculated. Typical values of ε_{ssmax} and ε_{ss1000} inputted into our model are 1.0 and 0.05, respectively.

The parameter TotDisp is the total amount of basal-displacement that occurs immediately adjacent to the fault surface for a given model run. These displacements at the base of the thrust wedge simulate the extreme shearing related displacements that are observed along the thrust surfaces of large-scale shear zones; for example, the Moine thrust (White et al. 1982; Coward 1988; Holdsworth 1990), the Särv thrust (Gilotti and Kumpulainen 1986, 1992), and the Morcle nappe (Ramsay and Huber 1983).

We define tectonic contraction strain (ε_{tc}) as a horizontal, uniaxial shortening with the shortening direction contained within the FTB motion plane. In the model, ε_{tc} decreases away from the hinterland toward the foreland as is schematically illustrated in Fig. 5. There is an abundance of geological evidence showing an increase in horizontal shortening towards the hinterland of a deforming thrust wedge (Gwinn 1970;

Table 1 List of model parameters and abbreviations

γ	Shear strain
ε_{ss}	Octahedral shear strain due to simple shear
ε_{ssmax}	The simple shear strain directly at the thrust surface
ε_{ss1000}	The simple shear strain at 1000 meters normal distance form the thrust
ε_{tc}	Octahedral shear strain due to tectonic contraction
ε_{g}	Octahedral shear strain due to gravity
ε_{g15k}	Gravitational strain at 15 km depth
ε_{rxn}	Octahedral shear strain due to the reaction force perpendicular to the fault
ε_{bv}	The amount of lateral confining stain needed to produce a plane strain
ε_{BC}	The lateral confining boundary strain
ε_{bvmax}	The maximum lateral boundary strain allowed in a given model run
TotDisp	Total amount of basal-displacement
nd	Normal distance from thrust
n_{inc}	The number of increments in a given model run
D_{inc}	The distance of basal-displacement for each increment
F	Deformation matrix (e.g., F_{inc} an incremental deformation matrix)
F_{2D}	The two-dimensional deformation matrix
L	Velocity gradient matrix (e.g., L_{hv} in the horizontal-vertical reference frame)
$\varepsilon_a, \varepsilon_b, \varepsilon_c$	Diagonal components of the L_{hv}
R_ϕ	Rotation matrix
ϕ	The dip of the fault within a given domain
EM	Ellipsoid matrix

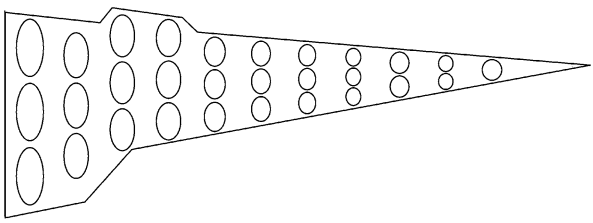

Fig. 5 A schematic diagram of how the tectonic contraction strain, ε_{tc}, varies throughout our wedge. This wedge has a vertical exaggeration of 2× that of our model wedge

Coward and Kim 1981; Price 1981; Mitra 1994; Gray and Mitra 1999). As with all the strain components, ε_{tc} is proportional to the size of the deformation increment and is also proportional to the amount of displacement for a given increment. To vary the amount of ε_{tc} with respect to the position in the wedge (Fig. 5), we have assigned a proportionality (P) to relate ε_{tc} and the amount of displacement. P is dependent on the horizontal distance from the back of the wedge (d). $P(d)$ decreases linearly with increased distance (d) such that $d = 0$ at the rear of the wedge and increases toward the foreland. Furthermore, $P(d) = 0$ at the toe of the thrust wedge. To completely define this relationship, one other value for P needs to be input for some horizontal distance, d. Thus, we input the amount of tectonic contraction strain we might expect if a marker started at the rear of the wedge ($d = 0$) and traveled above the thrust a distance of TotDisp. Using this value, $P(0)$, combined with the zero condition at the

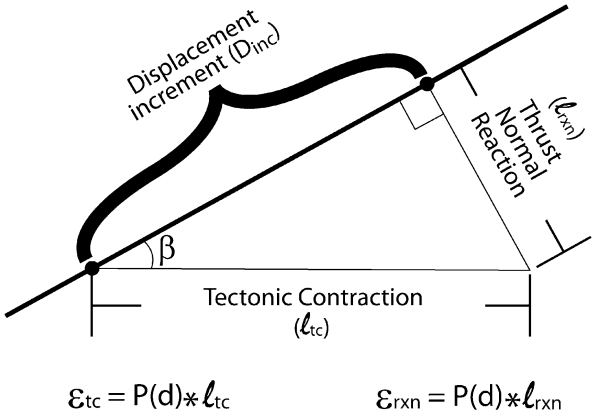

Fig. 6 The geometric relationship between the horizontal contraction length (l_{tc}), the thrust normal reaction length (l_{rxn}), and the fault dip (β) for a given displacement increment (D_{inc}). The horizontal contraction strain ($\varepsilon_{\mathrm{tc}}$) and the thrust normal reaction strain ($\varepsilon_{\mathrm{rxn}}$) are dependent on these respective lengths

wedge toe, the linear relationship for $P(d)$ can be completely defined. A value of 0.7 (octahedral shear strain) for $P(0)$ with a TotDisp value of 30 km is typically used.

In addition to $\varepsilon_{\mathrm{tc}}$, we also consider a thrust normal reaction strain which is related to $\varepsilon_{\mathrm{tc}}$. Given a dipping fault, not all of the tectonic contraction will go into shortening the rock horizontally because some of the deformation will be "re-directed" such that there is a component of the shortening that is directed normal to the fault. As Newton's third law of motion dictates, pushing against the fault will cause the fault to push back, resulting in what we call a thrust-normal reaction strain ($\varepsilon_{\mathrm{rxn}}$). Thus, there is a relationship between the tectonic contraction strain ($\varepsilon_{\mathrm{tc}}$), the thrust normal reaction strain ($\varepsilon_{\mathrm{rxn}}$), and the dip of the fault (β). This relationship needs to account for the two end-member cases of $\beta = 0°$, and $\beta = 90°$. At $\beta = 0°$, there would be no reaction strain because the contractional forces are directed parallel to the thrust surface. At $\beta = 90°$, both $\varepsilon_{\mathrm{tc}}$ and $\varepsilon_{\mathrm{rxn}}$ should go to infinity because movement along the fault from a horizontally directed force has become impossible. We have chosen to define this link between $\varepsilon_{\mathrm{tc}}$ and $\varepsilon_{\mathrm{rxn}}$ with the geometric relationship illustrated in Fig. 6. For a given incremental displacement amount (D_{inc}), a tectonic contraction length (l_{tc}) and thrust normal reaction length (l_{rxn}) can be solved for: $l_{\mathrm{tc}} = D_{\mathrm{inc}}/\cos[\beta]$; $l_{\mathrm{rxn}} = D_{\mathrm{inc}} \cdot \tan[\beta]$. These two lengths can be used in conjunction with $P(d)$ to determine $\varepsilon_{\mathrm{tc}}$ and $\varepsilon_{\mathrm{rxn}}$ using the simple formulas $\varepsilon_{\mathrm{tc}} = P(d) \cdot l_{\mathrm{tc}}$ and $\varepsilon_{\mathrm{rxn}} = P(d) \cdot l_{\mathrm{rxn}}$.

The relative importance of gravitational strains within tectonic environments has not been made clear within naturally deformed rocks. In fact, the effect of gravity is often ignored during strain analysis. It is a relatively straightforward calculation to estimate the stresses due to gravity at any given depth if one makes the simplifying assumption that the density and Poisson's ratio for the overlying rocks remains constant with depth (Means 1976). However, the relationship between these stresses and their associated strains is not straightforward. To relate stress to strain, one needs to assume a flow law. However, flow laws will vary dramatically with depth and the associated changes in temperature and pressure (Griggs et al. 1960; Handin et al. 1963; Donath 1970; Gleason and Tullis 1995). The exact relationship between temperature and pressure and a given flow law is not known. Therefore, we have made the simplifying assumption that gravitational strain (ε_{g}) varies linearly with depth. While our

linear assumption is certainly an over-simplification, this assumption is more geologically realistic than ignoring gravitational strain altogether. Moreover, we consider the linear assumption is more realistic than assuming a constant flow law for the entire wedge coupled with assumptions of constant rock-density and Poisson's ratio. We define ε_g as the octahedral shear strain associated with a vertically-oriented, uniaxial shortening. Assuming that $\varepsilon_g = 0$ at the surface of the wedge, then all we need to input into our model is the slope (α_g) of the line that relates ε_g with depth. Instead of inputting α_g directly, we input a value of octahedral shear strain associated with an overburden of 15 km, ε_{g15k}; typically a value of 0.08 is chosen. Using ε_{g15k}, we then calculate α_g thus defining the relationship between ε_g and depth. The last geologic input parameter is ε_{bvmax}, the maximum amount of lateral confining strain allowed within a given model run is discussed in more detail below.

2.3 Assembly of the Model Wedge and Initial Displacement profile

Once all the input data is entered into the program, the geometric input data is used to calculate all of the remaining wedge-shape parameters and construct the model wedge (Fig. 3). Next, we calculate the position along the thrust surface of the wedge where the base of each incremental line of observation markers will be positioned. The spacing between the individual basal markers is simply TotDisp/n_{inc}, where n_{inc} is the number of increments. This represents the incremental amount of basal-displacement. The observation markers above the basal marker will ultimately be displaced farther than the incremental slip amount due to internal distortion of the thrust sheet. The position of the first basal marker is dependent on Dth, the vertical height above the thrust surface to the top of the initial line of observation markers, and the dip of the fault, β (Fig. 3). Knowing the positions of the top and bottom of the initial line of markers, as well as the number of markers for a given model run, allows us to determine the initial position for each of the observation markers. Because the observation markers are initially oriented in a line that is perpendicular to the thrust surface, they are useful for tracking the displacement of material points within the deforming wedge. We refer to these distorted lines of observation markers as displacement profiles. This situation is analogous to the distortion of an initially vertical drill hole within an actively flowing glacier with a horizontal base.

The displacement profile is most easily observed within its own reference frame where the fault surface is the horizontal axis; this reference frame is called the profile-space. Within profile-space, the material paths of the observation markers are calculated and then transformed back into the reference frame for the deforming wedge, or wedge-space. Once the initial position of all the observation markers is determined (in both profile and wedge-space), the finite deformation matrices for each of these initial markers must be set to identity; in other words, the observation markers must start out as undeformed spheres.

The transformation between wedge space and profile space is typically a simple rotation operation. However, if the displacement profile passes through a kink boundary, a second rotation must be performed at the intersection of the kink boundary and a projected line connecting the two markers from the displacement profile closest to the kink boundary and on opposite sides of the boundary. No additional deformation

is associated with passing through the kink boundary in the model. While we understand that this is not geologically realistic, we consider it a necessary simplification at this stage in the development of the model, particularly in light of our goal of understanding first-order strain distribution patterns within deforming thrust wedges. Translating between profile-space and wedge space must be accomplished on a point-by-point basis because the position of each observation marker in wedge-space determines the deformation matrix used to calculate the incremental displacements within profile-space. The position for each observation marker is influenced by the displacements of all the markers beneath it. Thus, it is necessary to continually go back and forth between profile-space and wedge-space.

2.4 While Loops and Defining Strain Components

The primary function of the numerical model is to calculate the strain and strain paths of a series of observation markers. This is accomplished by utilizing two nested While loops (Fig. 2). The first/external While loop continues to run until the prescribed number of increments has elapsed. The second/internal While loop runs until all of the observation markers for a given increment have had their deformation matrices and associated strain calculations performed. The combined effect is that each observation marker for each increment successively undergoes a series of calculations which simulate progressive deformation through space and time.

Once inside the nested While loops, the first calculation assigns a domain number for each observation marker, where Domain 1 is within the lowermost thrust flat segment, Domain 2 is within the thrust ramp segment, and Domain 3 is within the uppermost flat segment. These domains are separated by kink boundaries (Fig. 3). It is important to monitor whether any given marker changed domains from the previous increment or even during an intermediate displacement within an increment because the appropriate rotations must be applied when a marker passes through a kink boundary.

Once the domains are known, l_{tc} and l_{rxn} can be calculated. If a marker passes through a kink boundary, these calculations become somewhat more involved and ultimately give rise to the separation of the increment into two sub-increments. Using l_{tc} and l_{rxn}, ε_{tc} and ε_{rxn} are calculated for a given observation marker with a horizontal position, d. The gravitational strain, ε_g, is calculated after determining the depth of the observation marker. Similarly, ε_{ss} is calculated once the normal distance away from the thrust is determined for the observation marker. From ε_{ss}, shear strain, γ, can be calculated using the relationship

$$\gamma = \frac{e^{\sqrt{2}\cdot\varepsilon_{ss}} - 1}{\sqrt{e^{\sqrt{2}\cdot\varepsilon_{ss}}}},$$

which is derived in Appendix.

2.5 Assembling the Incremental Deformation Matrix

Using the four strain components $\varepsilon_{tc}, \varepsilon_{rxn}, \varepsilon_g, \gamma$, a velocity gradient matrix can be assembled by assuming time = 1 (Ramberg 1975; Means 1976). First, the strain

components are grouped according to their reference frames. Since ε_{g} is vertically oriented and $\varepsilon_{\mathrm{tc}}$ is horizontally oriented, they can be considered to be in the same reference frame. Since the orientations of $\varepsilon_{\mathrm{rxn}}$ and γ are both dependent on the orientation of the fault, they can be considered to have the same reference frame. Strain components ε_{g} and γ need to be normalized by the number of deformation increments, n_{inc}. $\varepsilon_{\mathrm{rxn}}$ and $\varepsilon_{\mathrm{tc}}$ are already normalized by n_{inc} because D_{inc} (which equals $\mathrm{TotDisp}/n_{\mathrm{inc}}$) is incorporated into their formulations. A velocity gradient matrix that incorporates both horizontal and vertical uniaxial shortening will take the form

$$L_{\mathrm{hv}} = \begin{bmatrix} \varepsilon_a & 0 & 0 \\ 0 & \varepsilon_b & 0 \\ 0 & 0 & \varepsilon_c \end{bmatrix},$$

where for our model $\varepsilon_a = \varepsilon_{\mathrm{g}}$, $\varepsilon_b = \varepsilon_{\mathrm{g}} + \varepsilon_{\mathrm{tc}}$, and $\varepsilon_c = \varepsilon_{\mathrm{tc}}$. A velocity gradient matrix that incorporates horizontal simple shear and vertical shortening has the form

$$L_{\mathrm{f}} = \begin{bmatrix} \varepsilon_{\mathrm{rxn}} & 0 & \gamma \\ 0 & \varepsilon_{\mathrm{rxn}} & 0 \\ 0 & 0 & 0 \end{bmatrix} \quad \text{(Ramberg 1975)}.$$

To transform this velocity gradient matrix into the "horizontal-vertical" reference frame we must pre- and post-multiply this matrix by the rotation matrix R_ϕ and the transpose of R_ϕ, respectively, where

$$R_\phi = \begin{bmatrix} \cos[\phi] & 0 & \sin[\phi] \\ 0 & 1 & 0 \\ -\sin[\phi] & 0 & \cos[\phi] \end{bmatrix}$$

and ϕ is the dip of the fault within a given domain. Thus, $L_{\mathrm{frot}} = [R_\phi] \cdot [L_{\mathrm{f}}] \cdot [R_\phi]^{\mathrm{T}}$. By adding together the two separate reference frame velocity gradient matrices, L_{hv} and L_{frot}, we produce the total velocity gradient matrix for the deformation within the "horizontal-vertical" reference frame:

$$L_{\mathrm{tot}} = \begin{bmatrix} \varepsilon_{\mathrm{g}} + \varepsilon_{\mathrm{rxn}} \cdot \cos^2[\phi] - \gamma \cdot \cos[\phi] \cdot \sin[\phi] & 0 & \gamma \cdot \cos^2[\phi] + \varepsilon_{\mathrm{rxn}} \cdot \cos[\phi] \cdot \sin[\phi] \\ 0 & \varepsilon_{\mathrm{g}} + \varepsilon_{\mathrm{tc}} + \varepsilon_{\mathrm{rxn}} & 0 \\ -\gamma \cdot \sin^2[\phi] + \varepsilon_{\mathrm{rxn}} \cdot \cos[\phi] \cdot \sin[\phi] & 0 & \varepsilon_{\mathrm{tc}} + \varepsilon_{\mathrm{rxn}} \cdot \sin^2[\phi] + \gamma \cdot \cos[\phi] \cdot \sin[\phi] \end{bmatrix}$$

(Ramberg 1975).

However, the velocity gradient matrix does not allow us to determine kinematic parameters of interest (e.g., octahedral shear strain, the orientations of principal strain axes, Lode's ratio, etc.). A more useful tensor quantity for calculating such parameters is the deformation matrix. Unfortunately, it is considerably more difficult to combine instantaneous deformation matrices. Therefore, we assemble the velocity gradient matrix, where it is relatively easy to combine the various components of deformation, and then solve for the deformation matrix using the differential equation: $L \cdot F = F'$, where L is the velocity gradient matrix and F is the deformation matrix

(Bowen 1989). The resulting deformation matrix is

$$F = \begin{pmatrix} \frac{1}{2}\Lambda\left(1+e^{\frac{\Omega}{\sqrt{2}}} - \frac{(-1+e^{\frac{\Omega}{\sqrt{2}}})(\sqrt{3}(\varepsilon_{\mathrm{tc}}-\varepsilon_{\mathrm{g}}-\varepsilon_{\mathrm{rxn}}\cdot\cos[2\phi])+\sqrt{2}\cdot\gamma\cdot\sin[2\phi])}{\Omega}\right) & 0 & \\ 0 & e^{\frac{\varepsilon_{\mathrm{tc}}+\varepsilon_{\mathrm{g}}+\varepsilon_{\mathrm{rxn}}}{\sqrt{6}}} & \\ \frac{\Lambda(-1+e^{\frac{\Omega}{\sqrt{2}}})\sin[\phi]\cdot(\sqrt{3}\varepsilon_{\mathrm{rxn}}\cdot\cos[\phi]-\sqrt{2}\cdot\gamma\cdot\sin[\phi])}{\Omega} & 0 & \\ \frac{\Lambda(-1+e^{\frac{\Omega}{\sqrt{2}}})\cdot\cos[\phi]\cdot(\sqrt{2}\cdot\gamma\cdot\cos[\phi]+\sqrt{3}\cdot\varepsilon_{\mathrm{rxn}}\cdot\sin[\phi])}{\Omega} & & \\ 0 & & \\ \frac{\Lambda((1+e^{\frac{\Omega}{\sqrt{2}}})\cdot\Omega+(-1+e^{\frac{\Omega}{\sqrt{2}}})(\sqrt{3}(\varepsilon_{\mathrm{tc}}-\varepsilon_{\mathrm{g}}-\varepsilon_{\mathrm{rxn}}\cdot\cos[\phi])+\sin[2\phi]))}{2\Omega} & & \end{pmatrix},$$

where

$$\Omega = \sqrt{\left(3\left(\left(\varepsilon_{\mathrm{tc}}-\varepsilon_{\mathrm{g}}\right)^2+\varepsilon_{\mathrm{rxn}}^2\right)-2(\varepsilon_{\mathrm{tc}}-\varepsilon_{\mathrm{g}})\cdot\left(3\cdot\varepsilon_{\mathrm{rxn}}\cdot\cos[2\phi]-\sqrt{6}\cdot\gamma\cdot\sin[2\phi]\right)\right)}$$

and

$$\Lambda = e^{-\frac{\sqrt{3}\cdot(\varepsilon_{\mathrm{tc}}+\varepsilon_{\mathrm{g}}+\varepsilon_{\mathrm{rxn}})+3\Omega}{6\sqrt{2}}}.$$

Ω and Λ have no physical meaning and are only used for spatial parsimony. The deformation matrix has been constructed in such a way as to insure a constant volume deformation. This matrix has indeterminate components for the case where $\varepsilon_{\mathrm{rxn}} = 0$ and $\varepsilon_{\mathrm{g}} = \varepsilon_{\mathrm{tc}}$ because Ω will equal zero, and therefore the denominators of the 11, 13, 31, and 33 elements will also equal zero. For this special case, we need to use a simplified form of the deformation matrix, where

$$F = \begin{pmatrix} -\frac{1}{2}\cdot e^{\frac{-\varepsilon_{\mathrm{tc}}}{\sqrt{6}}}\cdot(-2+\gamma\cdot\sin[2\phi]) & 0 & e^{\frac{-\varepsilon_{\mathrm{tc}}}{\sqrt{6}}}\cdot\gamma\cdot\cos^2[\phi]) \\ 0 & e^{\sqrt{\frac{2}{3}}\cdot\varepsilon_{\mathrm{tc}}} & 0 \\ -e^{\frac{-\varepsilon_{\mathrm{tc}}}{\sqrt{6}}}\cdot\gamma\cdot\sin^2[\phi] & 0 & \frac{1}{2}\cdot e^{\frac{-\varepsilon_{\mathrm{tc}}}{\sqrt{6}}}\cdot(2+\gamma\cdot\sin[2\phi]) \end{pmatrix}.$$

In the context of our model, F constitutes an increment of the total deformation for a given observation marker referred to as F_{inc}.

2.6 Lateral Confining Boundary Conditions

The deformation matrix that has been calculated at this stage within the model has not incorporated any lateral confining boundary condition. We assume that our lateral boundary condition can only stop or hinder material from moving laterally out but cannot actively push in, i.e., no shortening occurs in the lateral direction. We accept that there are deformation environments that do produce lateral shortening, but we will not be addressing those boundary conditions at this stage within our model. To determine the maximum possible lateral confining strain, we calculate how much uniaxial shortening, directed perpendicular to the motion plane (i.e., the plane that

contains the slip vector and is perpendicular to the fault surface) is necessary to make the deformation plane strain, which we call $\varepsilon_{\mathrm{bv}}$. Because we cannot solve for $\varepsilon_{\mathrm{bv}}$ symbolically, we use the numerical bisection method to find the root of the equation $f(\varepsilon_{\mathrm{lc}}) = k(\varepsilon_{\mathrm{lc}}) - 1$, where $k(\varepsilon_{\mathrm{lc}})$ is the Flinn's k-value for a given incremental deformation with an applied lateral confining strain, $\varepsilon_{\mathrm{lc}}$. The quantity k is defined such that $k = 1$ is a plane strain deformation (Flinn 1962). Therefore, $f(\varepsilon_{\mathrm{lc}})$ will equal zero when an $\varepsilon_{\mathrm{lc}}$ is applied that produces a plane strain ellipsoid. The numerical "find root" algorithm quits once a predetermined amount of precision has been achieved (input into the model in the model-run input parameter section); typically a precision value of 10^{-7} such that $f(\varepsilon_{\mathrm{lc}}) < \pm 10^{-7}$ is used.

An additional complication in determining $\varepsilon_{\mathrm{bv}}$ is that there are multiple $\varepsilon_{\mathrm{lc}}$ values that satisfy the equation $k(\varepsilon_{\mathrm{lc}}) = 1$. The reason for this is that there are three possible plane strain ellipsoids for the orthogonal reference frame that we have chosen; in other words, each reference plane (a plane that contains two of the reference axes) could be a plane strain plane (the plane which contains all the material motion vectors during plane strain deformation). What this means for the numerical "find root" method is that the function can cross the origin up to three times; therefore, our algorithm must solve for a particular root, evaluate whether it is the appropriate root, and if it is not, continue to increase $\varepsilon_{\mathrm{lc}}$ until the appropriate plane strain ellipsoid is found. For the case of thrust systems, the appropriate plane strain ellipsoid will exhibit plane strain parallel to the motion plane (defined above). A common scenario is to obtain a prolate ellipsoid (where $1 < k < \infty$) whose long axis is perpendicular to the motion plane. In this case, the first plane strain ellipsoid achieved by adding increasing amounts of $\varepsilon_{\mathrm{lc}}$ will continue to have its long axis perpendicular to the motion plane. By continuing to increase $\varepsilon_{\mathrm{lc}}$, another plane strain ellipsoid will be achieved, one whose long axis is within the motion plane. Thus, $\varepsilon_{\mathrm{bv}}$, the amount of lateral confining strain needed to make the deformation plane strain, is calculated.

One of our geologic input parameters is the term $\varepsilon_{\mathrm{bvmax}}$, which we define as the maximum amount of lateral confining strain allowed for a given model run. If $\varepsilon_{\mathrm{bv}}$ is less than or equal to $\varepsilon_{\mathrm{bvmax}}$, then the lateral confining boundary condition, $\varepsilon_{\mathrm{BC}}$, will equal $\varepsilon_{\mathrm{bv}}$ and the deformation will be plane strain (for that specific marker and that particular increment) (Fig. 7). However, if $\varepsilon_{\mathrm{bv}}$ is greater than $\varepsilon_{\mathrm{bvmax}}$, then the lateral confining strain is capped at the value $\varepsilon_{\mathrm{bvmax}}$. After determining a value for the lateral confining strain component, $\varepsilon_{\mathrm{BC}}$, it can be incorporated into the incremental deformation matrix such that $\varepsilon_a = \varepsilon_{\mathrm{g}} + \varepsilon_{\mathrm{BC}}$ and $\varepsilon_c = \varepsilon_{\mathrm{tc}} + \varepsilon_{\mathrm{BC}}$; ε_b and γ will remain unchanged.

2.7 The Displacement Profile

Once the incremental deformation matrix, F_{inc}, is assembled, we use the corner components of that matrix to assemble the two-dimensional deformation matrix, F_{2D}. F_{2D} is used to determine the movement of the particles that make up the displacement profile. In profile space, the observation markers are initially arranged into a vertical line of markers with its lowermost end at the origin (Fig. 8). The markers are numbered such that marker zero is at the fault surface (the horizontal axis in profile space) and the marker numbers increase successively above the fault. Using F_{2D},

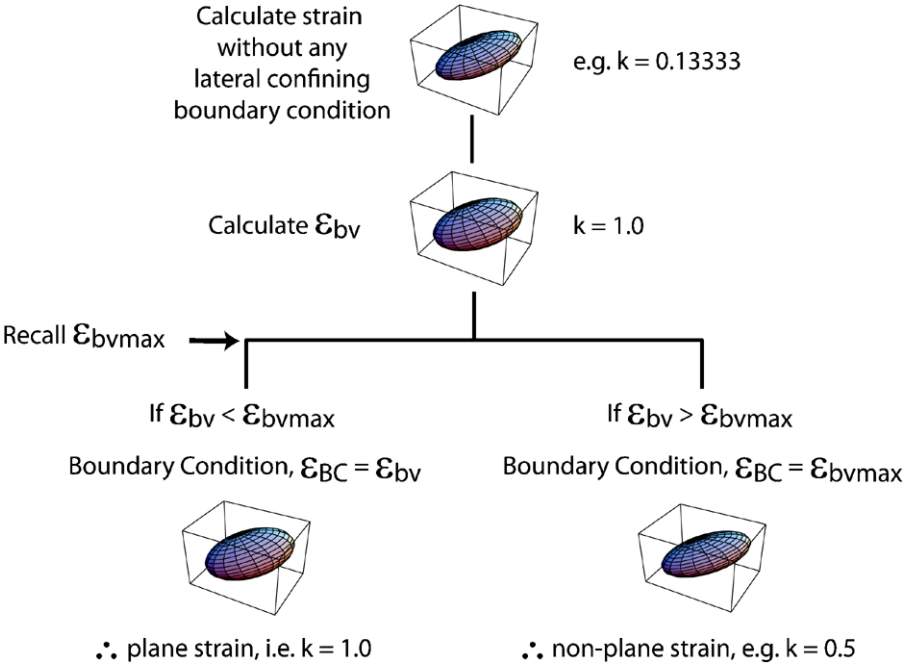

Fig. 7 A flow chart illustrating the process by which our numerical model determines the lateral confining strain, ε_{BC}

we can determine the displacement of observation marker #1 for the first increment of deformation by directly applying the deformation matrix to this marker's position matrix, $[F_{2D}] \cdot \{x, y\}$. However, for successive increments (and successive markers), the displacement vector is determined by applying F_{2D} to the matrix $\{0, h\}$, where h is the vertical distance between the marker of interest, $\#x$, and the marker directly beneath it, $\#x - 1$. This displacement vector can then be applied to the observation marker's initial position, yielding the displaced position for that given increment. The marker directly above this displaced marker, marker $\#x + 1$, is assumed to have moved passively with marker $\#x$ which yields an intermediate position for marker $\#x + 1$ (Fig. 8). The intermediate position of marker $\#x + 1$ is determined in wedge-space as well as profile space. The intermediate position in wedge-space is used to determine the depth, the horizontal position, and the normal distance away from the thrust; this ultimately determines the deformation matrix for that given increment (as described above). This process can then be repeated for each successive observation marker which then determines the material path for each of the markers, yielding a displacement profile. This approach assumes that each increment of deformation starts at the fault and propagates away from the fault surface. While this assumption is invariably inaccurate in detail, the inaccuracy is minimized by increasing the number of increments within the model and therefore decreasing the size of each individual increment. Again, it is important to keep track of which domain a particular observation marker is in and if it crosses into a new domain during these intermediate movements.

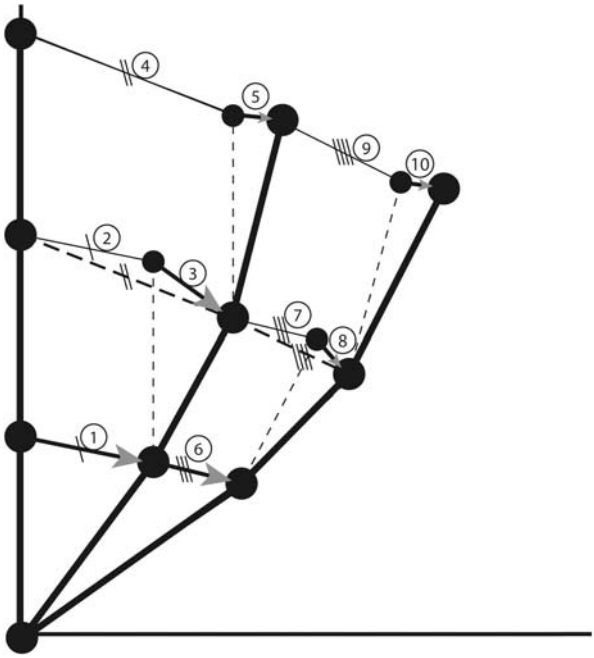

Fig. 8 A schematic illustration of how our displacement profiles are constructed. Displacement proceeds from the *bottom* to the *top*. After an observation marker is displaced, the marker directly above it is passively displaced by the same amount before that marker is displaced by its own deformation matrix. The *circled numbers* represent the order in which the displacements occur

2.8 Finite Strain Deformation Matrix

Finally, the incremental deformation matrix, F_{inc}, can be incorporated into the finite deformation matrix, F_{tot}, which tracks the sum of the deformation increments for a given observation marker. F_{inc} is incorporated by using the formula: $F_{\text{tot}}[\text{increment number}] = F_{\text{inc}}[\text{increment number}] \cdot F_{\text{tot}}[\text{increment number} - 1]$. From both the finite deformation matrix, F_{tot}, and the incremental deformation matrix, F_{inc}, we can calculate the ellipsoid matrix, EM, by $[\text{EM}_x] = [[F_x]^{-1}]^{\text{T}} \cdot [F_x]^{-1}$, where x is either tot or inc. The lengths of the principal axes of the strain ellipsoid, l_x, can be determined by using the equation $l_x = \frac{1}{\sqrt{\lambda_x}}$, where λ_x are the eigenvalues of EM ($x = 1, 2$, or 3 which represent the maximum, intermediate, and minimum extension directions, respectively). The principal strain axes are parallel to the eigenvectors of EM which, combined with the principal lengths, uniquely defines the strain ellipsoid.

2.9 Graphical Representation of Wedge Kinematics

Once the While loops have finished (Fig. 2), both the finite and increment strain ellipsoids have been calculated and stored for each observation marker along with their position in the wedge for each increment. At this stage, strain parameters (octahedral shear strains, Lode's ratio, etc.) can be calculated from the strain ellipsoids and various aspects of the kinematics of the thrust wedge can be graphically represented. The program can output a series of either finite or incremental ellipsoid images (Fig. 9a). Since the program is written in Mathematica, it is easy to view a series of images as

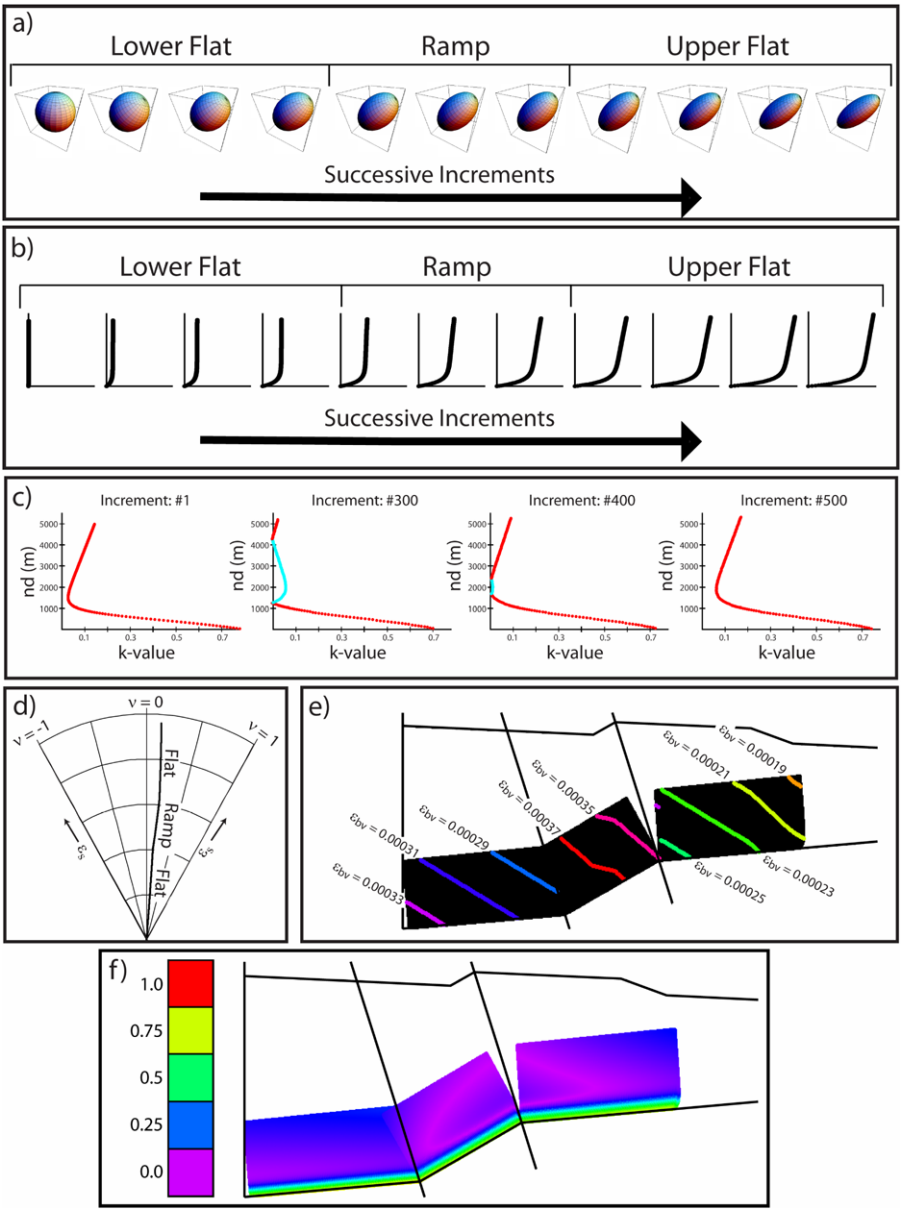

Fig. 9 Forms of graphical output for kinematic data from our numerical model: **a** progressive finite strain ellipsoids for successive increments of deformation for a given observation marker, **b** progressive displacement profiles for successive increments of deformation, **c** a series of Flinn's k-value versus normal distance from the thrust plots (nd) for increments 1, 300, 400, and 500 for a model run with 500 increments, **d** a Hsu diagram illustrating the strain path for a particular observation marker. Within the ramp segment the strain path deflects to the right, i.e., undergoes increased flattening, **e** our deforming thrust wedge. The *black portion is the area* in which the displacement profiles have traveled through. *Contour lines* are values of ε_{bv}, the amount of lateral confining strain needed to make the incremental deformation plane strain. ε_{bv} values increase within the ramp segment, **f** a series of 500 displacement profiles plotted in wedge-space. The individual observation markers are color-coded to values of Flinn's k-value

a movie of the deforming marker, which is a helpful visual supplement to the numerical data. Similarly, the displacement profiles can be viewed as a series of images in profile space which can then easily be viewed as a movie (Fig. 9b). We have found the profile movies particularly useful in noticing changes in trajectory and rates of particle movement associated with moving through the ramp segment of the thrust. Flinn's k-value (Flinn 1962) is a familiar parameter to most structural geologists; therefore, we have plotted k-values versus normal distance from the thrust for various increments (Fig. 9c). Again, a movie is a useful way to recognize changes in kinematics throughout the deformation history. While Flinn's k-value is more well-known, we consider the most useful diagram for examining strain path to be the Hsu diagram (Hsu 1966) which plots Lode's ratio (ν) (Hossack 1967) versus octahedral shear strain (ε_s) (Nadai 1963). The Hsu diagram consists of a 60° wedge segment of a circle where ε_s increases radially away from the apex of the wedge and ν ranges from -1 to 1 along the concentric arcs (Fig. 9d) (Hsu 1966). Lode's ratio is defined such that $\nu = -1$ for a perfectly prolate strain ellipsoid, $\nu = 0$ for plane strain, and $\nu = 1$ for a perfectly oblate strain ellipsoid (Hossack 1967). Another useful way to visualize wedge kinematics is to plot all of the displacement profiles in wedge space and then contour some value associated with the kinematics (e.g., ε_{bv}, Fig. 9e). Alternatively, we color-code each of the observation markers in the displacement profiles to some kinematic value (e.g., Flinn's k-value for the finite strain ellipsoids, Fig. 9f), allowing us to observe the kinematics of the entire wedge.

3 Mathematical Model Results

As the model is configured to compute strain data for a thrust wedge with a flat-ramp-flat geometry (although a simpler wedge geometry can be input by setting $\Gamma = \beta$ and hul = lul = 0, Fig. 3), we first examine the difference between flat and ramp kinematics. For instance, there is a difference in the general material path within the ramp segment, when compared to the adjacent flats. The displacement profile tends to increase in height within the flat segments and decrease in height within the ramp segment. This difference reflects variable amounts of horizontal contraction versus thrust normal reaction strain. In the more steeply dipping ramp segment, the tectonic forces are pushing harder against the fault surface, generating greater flattening strains which are reflected in the vertically shortened displacement profile. A similar trend can be observed within Hsu diagrams. The Hsu diagram allows one to observe the strain path for a given observation marker (Hsu 1966). In Fig. 9d, the Hsu diagram demonstrates that when the marker enters the ramp segment, there is an increase in the amount of flattening strain (i.e., the strain path gets deflected to the right, toward $\nu = 1$, oblate strain geometry). When the observation marker leaves the ramp segment the strain path deflects again, this time toward the left.

One of the major concerns in developing the numerical model was how to incorporate realistic lateral boundary conditions. Many numerical models make the simplifying assumption that deformation takes place by plane strain (Willet 1992, 1999; Erickson and Jamison 1995; Strayer and Hudleston 1997, 1998; Smart et al. 1999).

On the other hand, there is an abundant amount of data from thrust wedge environments which demonstrate that a plane strain assumption is not realistic in detail (Durney and Ramsay 1973; Geiser 1988; Mukul and Mitra 1998; Twiss and Unruh 1998; Gray and Mitra 1999; Strine and Mitra 2004). However, incorporating no lateral boundary condition is even less realistic. What, then, is a realistic value for the lateral confining boundary condition? This question would be considerably difficult, if not impossible, to address with only finite strain data collected from naturally deformed rocks. However, a realistic forward model combined with significant amounts of field data may be able to give reasonable estimates of lateral boundary conditions. A series of models with gradually increasing amounts of maximum lateral confining strain, $\varepsilon_{\text{bvmax}}$, was run and the strain patterns that vary as a function of $\varepsilon_{\text{bvmax}}$ were observed. With little or no lateral confining strain much of the thrust wedge will have finite strain ellipsoids with their long axes perpendicular to the motion plane (Fig. 10). The reason for this is that the vertical gravitational strain, the horizontal contraction strain and the thrust normal reaction strain all have components of extension normal to the motion-plane. Unlike the extension directions within the motion plane, these extension directions are all parallel, and therefore constructively reinforce one another. As a result, the maximum extension direction for the combination of these three strain components is perpendicular to the motion plane. The lateral confining boundary condition competes against extension in this direction (Fig. 1). Figure 10 illustrates the effect of increasing $\varepsilon_{\text{bvmax}}$ on the orientation of the maximum extension direction (i.e., whether it is perpendicular or parallel to the transport direction). When there is little or no lateral confining strain, the only place within the wedge that has transport parallel maximum extension directions is near the thrust surface where the deformation is being dominated by simple shear deformation. As $\varepsilon_{\text{bvmax}}$ increases, more of the finite strain ellipsoids within the wedge have their long axes oriented parallel to the transport direction until the entire wedge has transport parallel long axes. Note that the area within the wedge that is most likely to have transport perpendicular long axes is the ramp segment. This is demonstrated in Fig. 10b where the finite strains do not switch to being transport-perpendicular until they reach the ramp segment and eventually switch back to being transport-parallel within the upper flat. This situation illustrates the idea that hanging wall rocks carry with them the sum of their deformation histories which could contain such complexities as traveling over flat–ramp–flat fault geometry.

It is also useful to examine the strain patterns within the deforming wedge. The finite strains increase from left to right with progressive deformation as well as increasing closer to the thrust surface, as one would expect (Fig. 11a). It is somewhat more illustrative to examine the incremental strain patterns (Fig. 11b). In general, the incremental strains also increase closer to the thrust surface. In addition, the incremental strain data demonstrates an increase in strain magnitudes within the ramp segments. Therefore, not only do the hanging wall markers record increased flattening strain geometries from the ramp segment, but because of the increase in strain magnitude, those "ramp-strains" could have a significant influence on the finite strain magnitudes and geometries.

The interplay of the various strain components will determine the strain geometry for a given observation marker. As discussed above, one way to characterize

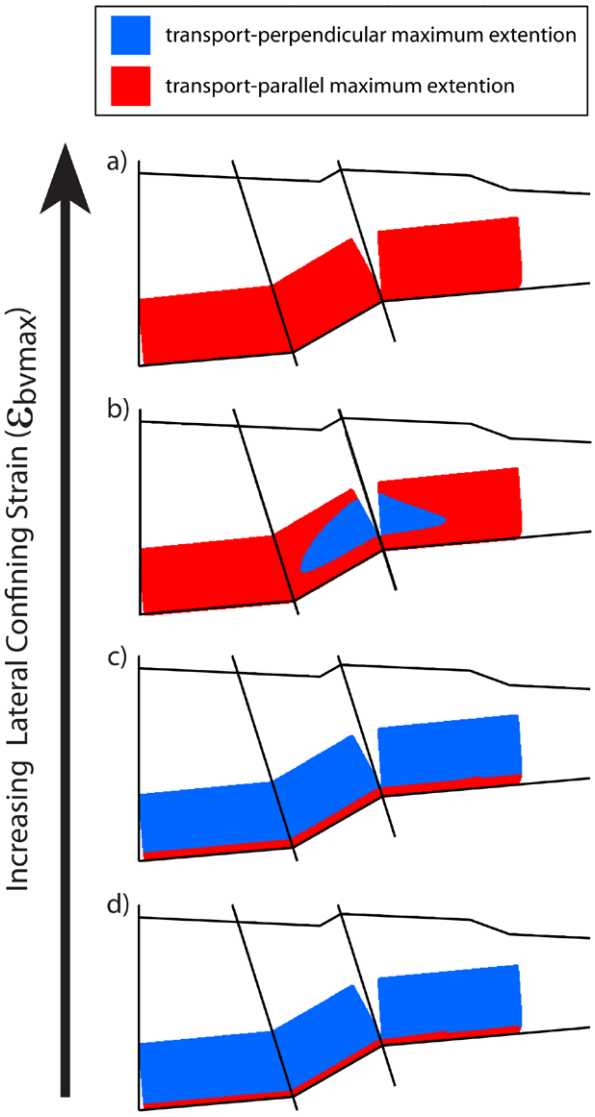

Fig. 10 A series of models runs where the maximum amount of lateral confining strain, $\varepsilon_{\text{bvmax}}$ is varied. Each wedge includes a series of 500 displacement profiles. The *red region* represents observation markers with finite strain ellipsoid long axes that lie within the motion plane. The *blue regions* represent finite strain ellipsoids with their long axes perpendicular to the motion plane: **a** $\varepsilon_{\text{bvmax}} = 0.1425$, **b** $\varepsilon_{\text{bvmax}} = 0.095$, **c** $\varepsilon_{\text{bvmax}} = 0.0475$, **d** $\varepsilon_{\text{bvmax}} = 0.0$

strain geometry is with Flinn's k-value (Flinn 1962). Therefore, k-values were plotted against the normal distances from the thrust surface for each increment (Fig. 9c). From these plots, one can observe that the k-values are at a maximum closest to the fault. This is due to the predominance of simple shear deformation (which is a plane strain deformation, $k = 1$) near the fault surface. In general, for markers farther away from the fault surface, the k-values decrease until they reach some minimum value and then begin to increase (Fig. 9c). This minimum k-value changes with position in the wedge and is therefore a function of the relative proportions of the various strain components. The k-value pattern is somewhat complicated by the existence of the fault ramp. At the ramp, the k-values dramatically decrease. Once they reach a value

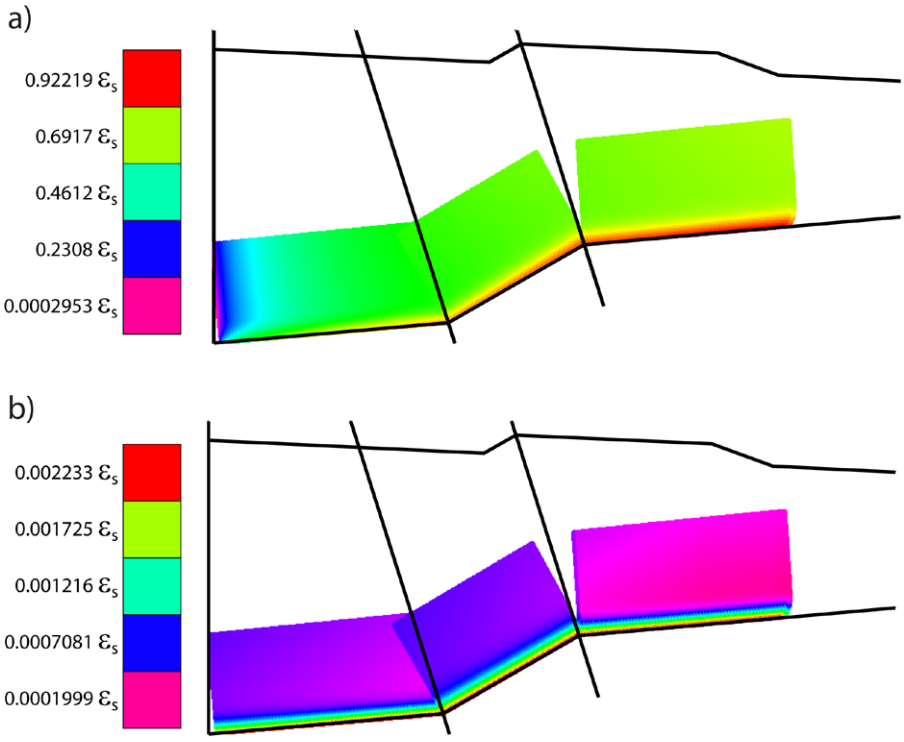

Fig. 11 Finite **a** and incremental **b** strains within a deforming thrust wedge. Each wedge includes a series of 500 displacement profiles color-coded to values of octahedral shear strains, ε_S

of zero, they start to increase again. This represents the situation where the long axis of the strain ellipsoid switches from being transport parallel to transport perpendicular. Once the deformation profile has reached the upper flat, the "switched" k-values will begin to decrease and the "non-switched" k-values will begin to increase. Similar results can be observed by viewing the wedge diagram where the observation markers have been color-coded to values of k. Figure 9f illustrates that the k-values are at a maximum near the thrust surface; they decrease away from the thrust to a minimum value and then begin to increase. One can also notice a kinked lozenge-shaped domain in the ramp and upper flat wedge segments. This domain is defined by a circuit of minimum k-values. Within this circuit, the k-values increase because these markers have switched from having transport parallel to transport perpendicular long axes (Fig. 10). In the upper flat portion of the wedge, the "switched" k-values decrease to zero and then start to increase from left to right, i.e., as deformation progresses and material moves up the thrust. Furthermore, all the transport-parallel observation markers within the upper flat have k-values that increase from left to right.

Another way of evaluating wedge kinematics is to examine the lengths of the individual strain axes. In particular, the length of the strain axis perpendicular to the motion plane (l_{perp}) can be useful for quantifying the amount of out-of-the-plane motion. Figure 12 illustrates both finite and incremental lengths of the motion-plane-

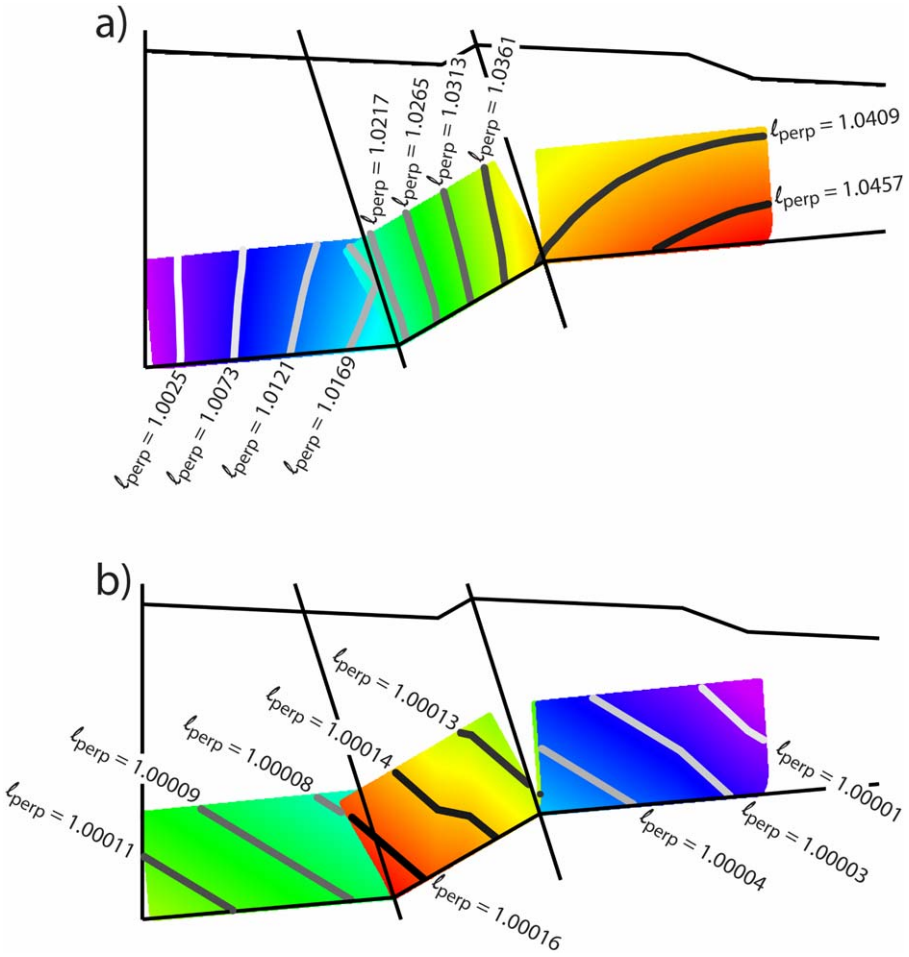

Fig. 12 Distribution of the out-of-the-plane motion for the finite **a** and incremental **b** strain ellipsoids throughout the deforming wedge. Each wedge includes a series of 500 displacement profiles contoured with respect to the length of the motion plane perpendicular strain axes, l_{perp}

perpendicular strain axes. Again, the incremental strain diagram is more useful for understanding the kinematic effects of the flat–ramp–flat geometry. Not surprisingly, the maximum perpendicular motion of markers is within the ramp segment. What may be surprising is where, within the ramp segment, the maximum perpendicular motion occurs. It is neither within the middle of the ramp segment where there is the greatest likelihood of having transport perpendicular long axes (Fig. 10b) nor in the center of the kinked lozenge defined by the minimum k-values (Fig. 9f). Instead it is where the depth is greatest within the ramp segment. This means that markers closer to the thrust with transport parallel long axes can have greater out-of-the-plane motion than markers farther from the thrust with transport perpendicular long axes. One should also notice the kinked geometry of the (l_{perp}) contours. These kinked regions are associated with kinks in the topographic surface, illustrating the influ-

ence of depth on out-of-the-plane motion. Since depth is only incorporated in the calculation of the gravitational strain, we recognize the potential for gravity to have a considerable influence on the strain patterns within a deforming wedge.

We consider ε_{bv}, the amount of confining strain needed to make any given incremental deformation plane strain, to be a useful kinematic parameter for this type of modeling. In Fig. 9d, the contours of ε_{bv} are shown within the model wedge. Again, notice a kink geometry to the contours which is associated with kinks in the topographic surface. It is intuitive that the amount of motion-plane-perpendicular shortening needed to make the deformation plane strain will be related to the initial lengths of the strain ellipsoid axis perpendicular to the motion plane. Therefore, the ε_{bv} patterns within the wedge are also strongly influenced by the gravitational strain component.

In the above examples, the values for ε_{tc}, ε_{ssmax}, ε_{ss1000}, and ε_{g15k} are held constant while varying ε_{bvmax}. However, it is also instructive to observe the consequences of varying each of these four parameters individually. Increasing ε_{tc} results in increased flattening throughout the wedge, increased perpendicular flow, and a greater number of transport-perpendicular maximum extension directions. The increased ε_{tc} also makes the kinks within the incremental perpendicular flow contours (Fig. 12b) less severe, suggesting that gravity is playing a relatively smaller roll in the deformation. By increasing either ε_{ssmax} or ε_{ss1000}, the amount of flattening near the thrust decreases, the strain magnitudes near the thrust increase, and the displacement profiles (Fig. 9b) become much more sheared out; they extend farther in the horizontal direction. Lastly, increasing ε_{g15k} causes an increase in the flattening strains, increased perpendicular flow, and a greater number of transport-perpendicular maximum extension directions. Furthermore, the increased ε_{g15k} also makes the kinks within the perpendicular flow contours more distinctive.

4 Conclusions

Using the conceptually simple technique of combining successive incremental deformation matrices, we have developed a useful mathematical model for understanding the kinematics of a deforming thrust wedge. Assumptions have been made about how several strain components (gravitational, contractional, thrust normal reaction, and simple shear strains) vary within a thrust wedge based on generally observed strain patterns within deforming FTB-wedges. Furthermore, we have imposed a lateral confining strain component, ε_{BC}, which is less than or equal to the amount of strain needed to make the deformation plane strain. Because there is no data available for appropriate magnitudes of this lateral boundary condition strain, we ran a series of models in which ε_{bvmax} was the only parameter that we varied. In this way, we have been able to calculate the incremental strains and assemble an incremental deformation matrix for any position within the wedge. By combining these incremental deformation matrices for the given observation markers within a deforming wedge, we can observe the strain paths for those markers. Our model has included a wedge with a flat–ramp–flat fault surface geometry. This enables us to examine the effects of this relatively common fault geometry on the kinematics of a deforming wedge.

Using the numerical model, some general predictions about the kinematics of a deforming FTB-wedge with a flat–ramp–flat geometry can be made. Multiple lines of evidence for greater flattening strains within the ramp segment of the wedge were observed. This flattening was manifest in the vertical shortening of the displacement profiles, the rightward deflection of the strain paths on the Hsu diagram, and the kinked lozenge shaped domain of minimum Flinn's k-values originating within the ramp segment. We also note that, in general, flattening strains increase away from the thrust surface (k-values decrease) to some minimum value at which point they tend to decrease (k-values increase). Furthermore, the incremental octahedral shear strains have relatively greater values within the ramp segment than the adjacent flats. The fault ramp is also the most likely region to observe transport perpendicular long axes for the finite strain ellipsoid given low to moderate lateral confining boundary conditions. Lastly, from the distribution of the strain axes that are oriented perpendicular to the motion plane and the contoured $\varepsilon_{\mathrm{bv}}$ patterns, we predict that gravitational strain can significantly affect the finite strain distribution within a deforming wedge, particularly with regards to out-of-the-plane motion.

Acknowledgements This work was supported by NSF grant EAR0208001 awarded to G. Mitra. This paper has benefited from useful conversations with Sanghoon Kwon as well as constructive comments and criticisms of early drafts of this manuscript from Jay Gates, and Shona Mookerjee. We also want to thank the anonymous reviews for their thoughtful comments and suggestions.

Appendix

A relatively simple relationship can be determined for the octahedral shear strain due to simple shear, $\varepsilon_{\mathrm{ss}}$, and the shear strain, γ. First, it is useful to determine a relationship between the axial ratio of a strain ellipse, R, and the associated γ. Using the deformation matrix for simple shear,

$$[\mathrm{SS}] = \begin{bmatrix} 1 & \gamma \\ 0 & 1 \end{bmatrix},$$

we can calculate the ellipse matrix, $[\mathrm{EM_{ss}}] = [[\mathrm{SS}]^{-1}]^{\mathrm{T}} \cdot [\mathrm{SS}]^{-1}$. Ramsay (1967) determined the relationship $\theta' = 0.5 \cdot \tan^{-1}[\frac{2}{\gamma}]$, where θ' is the angle between the shear surface and the long axis of the strain ellipse. Using θ', we can diagonalize EM with the rotation matrix

$$R_{\theta'} = \begin{bmatrix} \cos[\theta'] & -\sin[\theta'] \\ \sin[\theta'] & \cos[\theta'] \end{bmatrix}$$

such that $[\mathrm{EM_{diag}}] = [R_{\theta'}]^{\mathrm{T}} \cdot [\mathrm{EM_{ss}}] \cdot [R_{\theta'}]$. The square root of the diagonal components of $[\mathrm{EM_{diag}}]$ equals the lenghts of the principal axes of the strain ellipse. The axial ratio, R_{ss}, of the strain ellipse is the ratio of the major principal axis to the minor

principal axis. Therefore,

$$R_{ss} = \frac{\sqrt{2+\gamma^2\left(1+\sqrt{1+\frac{4}{\gamma^2}}\right)}}{\sqrt{2-\gamma^2\left(-1+\sqrt{1+\frac{4}{\gamma^2}}\right)}}. \tag{2}$$

Solving for γ yields

$$\gamma = \pm\frac{\sqrt{-(1+R_{ss})^2}}{\sqrt{R_{ss}}}, \tag{3}$$

$$\gamma = \pm\frac{i\sqrt{-(R_{ss}-1)^2}}{\sqrt{R_{ss}}}. \tag{4}$$

The solution for γ shown in equation (3) yields imaginary numbers for any real value of R_{ss}, thus we disregard this solution. The positive solution for equation (4) always yields a negative value for γ given a positive value for R_{ss}. To stay in keeping with typical sign convention, we eliminate this solution as well. This leaves the solution

$$\gamma = \frac{-i\sqrt{-(R_{ss}-1)^2}}{\sqrt{R_{ss}}}, \tag{5}$$

which simplifies to

$$\gamma = \frac{(R_{ss}-1)}{\sqrt{R_{ss}}}. \tag{6}$$

Our next step is to find a relationship between R_{ss} and ε_{ss}. The general equation for octahedral shear strain is $\varepsilon_s = \frac{1}{\sqrt{3}}\sqrt{(\varepsilon_1-\varepsilon_2)^2+(\varepsilon_2-\varepsilon_3)^2+(\varepsilon_3-\varepsilon_1)^2}$, where $\varepsilon_x = \mathrm{Ln}[\frac{l_x}{l_0}]$, ($x = 1, 2$, or 3 which represent the maximum, intermediate, and minimum extension directions, respectively), l_x equals the half-length of the principal axes and l_0 equals the initial radius of the undeformed sphere. Because simple shear deformation is plane strain, we know that $l_2 = l_0$, and therefore $\varepsilon_2 = 0$. Also, we can assume that the deformation maintains a constant volume. This assumption allows us to relate the lengths of the principal axes with their axial ratios. For plane strain deformation, we need only consider the axial ratio of the major and minor axes which are equivalent to the axial ratio we calculated in (2), R_{ss}. The area of the ellipse containing the major and minor axes will be equivalent to the area of a circle with a radius of l_0. Thus, the area, $A = \pi l_0^2 = \pi l_1 l_3$. Using the relationship $R_{ss} = \frac{l_1}{l_3}$, we can solve for l_1 and l_3 in terms of R_{ss} and A

$$l_1 = \sqrt{\frac{R_{ss}A}{\pi}}, \tag{7}$$

$$l_3 = \sqrt{\frac{A}{R_{ss}\pi}}. \tag{8}$$

Next, dividing equations (7) and (8) by l_0 yields

$$\frac{l_1}{l_0} = \sqrt{R_{ss}}, \tag{9}$$

$$\frac{l_3}{l_0} = \sqrt{\frac{1}{R_{ss}}}. \tag{10}$$

Plugging equations (9) and (10) into the equation for octahedral shear strain gives

$$\varepsilon_{ss} = \frac{1}{\sqrt{3}}\sqrt{\left(\mathrm{Ln}\left[\sqrt{R_{ss}}\right]\right)^2 + \left(\mathrm{Ln}\left[\frac{1}{\sqrt{R_{ss}}}\right]\right)^2 + \left(\mathrm{Ln}\left[\sqrt{R_{ss}}\right] - \mathrm{Ln}\left[\frac{1}{\sqrt{R_{ss}}}\right]\right)^2}, \tag{11}$$

which simplifies to

$$\varepsilon_{ss} = \frac{\sqrt{2}}{2}\mathrm{Ln}[R_{ss}]. \tag{12}$$

Solving for R_{ss} gives

$$R_{ss} = e^{\sqrt{2}\cdot\varepsilon_{ss}}. \tag{13}$$

Combining equation (13) with equation (6) yields

$$\gamma = \frac{e^{\sqrt{2}\cdot\varepsilon_{ss}} - 1}{\sqrt{e^{\sqrt{2}\cdot\varepsilon_{ss}}}}, \tag{14}$$

which is the relationship between shear strain, γ, and octahedral shear strain for simple shear, ε_{ss}.

References

Bowen RM (1989) Introduction to continuum mechanics for engineers. Plenum Press, New York, 261 p

Chapple WM (1978) Mechanics of thin-skinned fold-and-thrust belts. Geol Soc Am Bull 81:1189–1198

Coward MP (1988) The Moine thrust and the Scottish Caledonides. In: Mitra G, Wojtal S (eds) Geometries and mechanisms of thrusting, with special reference to the Appalachians. Geol Soc Am Spec Paper, vol 222, pp 1–15

Coward MP, Kim JH (1981) Strain within thrust sheets. In: McClay KR, Price (eds) Thrust and nappe tectonics, Special publication geological society London, vol 9, pp 275–292

Davis D, Suppe J, Dahlen F (1983) Mechanics of fold-and-thrust belts and accretionary wedges. J Geophys Res B 88:1153–1172

DeCelles PG, Mitra G (1995) History of the Sevier orogenic wedge in terms of critical taper models, northeast Utah and southwest Wyoming. Geol Soc Am Bull 107(4):454–462

Donath FA (1970) Some information squeezed out of rock. Am Sci 58:54–72

Durney DW, Ramsay JG (1973) Incremental strains measured by syntectonic crystal growth. In: DeJong KA, Scholten R (eds) Gravity and tectonics. Wiley, New York, pp 67–96

Erickson SG, Jamison WR (1995) Viscous-plastic finite-element models of fault-bend folds. J Struct Geol 17:561–573

Flinn D (1962) On folding during three-dimensional progressive deformation. Q J Geol Soc Lond 118:385–433

Fossen H, Tikoff B (1993) The deformation matrix for simultaneous pure shear, simple shear, and volume change, and its application to transpression/transtension tectonics. J Struct Geol 15:413–425
Geiser PA (1988) The role of kinematics in construction and analysis of geological cross sections in deformed terranes. In: Mitra G, Wojtal S (eds) Geometries and mechanisms of thrusting, with special reference to the Appalachians. Geol soc Am spec paper, vol 222, pp 47–76
Gilotti JA (1992) The rheologically critical matrix in arkosic mylonites along the Särv Thrust, Swedish Caledonides. In: Mitra S, Fisher GW (eds) Structural geology of fold and thrust belts (the Elliott volume). Johns Hopkins University Press, Baltimore, pp 145–160
Gilotti JA, Kumpulainen R (1986) Strain softening induced ductile flow in the Särv thrust sheet, Scandinavian Caledonides. J Struct Geol 8:441–455
Gleason GC, Tullis J (1995) A flow law for dislocation creep of quartz aggregates determined with the molten salt cell. Tectonophysics 247:1–23
Gray MB, Mitra G (1999) Ramifications of four-dimensional progressive deformation in contractional mountain belts. J Struct Geol 21:1151–1160
Griggs DT, Turner FJ, Heard HG (1960) Deformation of rocks at 500° to 800°C. In: Griggs DT, Handin J (eds) Rock deformation. Geol soc of Am memoir, vol 79, pp 39–104
Gwinn V (1970) Kinematic patterns and estimates of lateral shortening, Valley and Ridge and Great Valley provinces, central Appalachians, south-central Pennsylvania. In: Studies of Appalachian geology, central and southern. Interscience, New York, pp 127–146
Handin J, Hager RV Jr, Friedman M, Feather JN (1963) Experimental deformation of sedimentary rocks under confining pressure: pore pressure tests. Am Assoc Pet Geol Bull 47:717–755
Holdsworth RE (1990) Progressive deformation structures associated with ductile thrusts in the Moine Nappe, Sutherland, N. Scotland. J Struct Geol 12:443–452
Hossack JR (1967) Pebble deformation and thrusting in the Bygdin Area (southern Norway). Tectonophysics 5:315–339
Hsu TC (1966) The Characteristics of coaxial and non-coaxial strain paths. J Strain Anal 1:216–222
Jiang D, Williams PF (1998) High-strain zones; a unified model. J Struct Geol 20:1105–1120
Kwon S, Mitra G (2004) Three-dimensional finite-element modeling of a thin-skinned fold-thrust belt wedge; Provo Salient, Sevier Belt, Utah. Geology 32(7):561–564
Law RD (1987) Heterogeneous deformation and quartz crystallographic fabric transitions: natural examples from the Moine Thrust zone at the Stack of Glencoul, northern Assynt. J Struct Geol 9:819–834
Lin S, Jiang D, Williams PF (1998) Transpressional (or transtensional) zones of triclinic symmetry: natural example and theoretical modelling. In: Holdsworth RE, Strachan RA, Dewey JF (eds) Continental transpressional and transtensional tectonics. Special publication of the geological society of London, vol 135, pp 41–57
Means WD (1976) Stress and strain: Basic concepts of continuum mechanics for geologists. Springer, New York, 339 pp
Mitra G (1979) Ductile deformation zones in the Blue Ridge basement rocks and estimation of finite strains. Geol Soc Am Bull 90:935–951
Mitra G (1994) Strain variation in thrust sheets across the Sevier fold-and-thrust belt (Idaho–Utah–Wyoming): implications for section restoration and wedge taper evolution. J Struct Geol 16(4):585–602
Mitra G (1997) Evolution of salients in a fold-and-thrust belt: the effects of sedimentary basin geometry, strain distribution and critical taper. In: Sengupta S (ed) Evolution of geological structures from macro- to micro- scales. Chapman and Hall, London, pp 59–90
Mukul M, Mitra G (1998) Finite strain and strain variation analysis in the Sheeprock thrust sheet: an internal thrust sheet in the Provo salient of the Sevier fold-and-thrust belt, Central Utah. J Struct Geol 20:403–417
Nadai A (1963) Theory of flow and fracture of solids. Engineering societies monographs. McGraw-Hill, New York, 705 pp
Price RA (1981) The Cordilleran foreland thrust and fold belt in the southern Canadian Rocky Mountains. In: Price NJ, McClay KR (eds) Thrust and nappe tectonics. Geological society of London special publication, vol 9, pp 427–428
Ramberg H (1975) Particle paths, displacement and progressive strain applicable to rocks. Tectonophysics 28:1–37
Ramsay JG (1967) Folding and Fracturing of Rocks. McGraw-Hill, New York, 568 p
Ramsay JG, Graham RH (1970) Strain variations in shear belts. Can J Earth Sci 7:786–813
Ramsay JG, Huber MI (1983) The techniques of modern structural geology, vol 1. Academic Press, London, 462 p

Smart KJ, Kreig RD, Dunne WD (1999) Deformation behavior during blind thrust translation as a function of fault strength. J Struct Geol 21:855–874
Strayer LM, Hudleston PJ (1997) Simultaneous folding and faulting and fold-thrust belt evolution. In: A distinct element model. Geol. soc. of Am. abstracts with programs, vol 29/6, p A44
Strayer LM, Hudleston PJ (1998) Controls of duplex formation: results from numerical models. Geol soc of Am abstracts with programs, vol 30/7, p A42
Strayer LM, Suppe J (2002) Out-of-plane motion of a thrust sheet during along-strike propagation of a thrust ramp; a distinct-element approach. J Struct Geol 24(4):637–650
Strine M, Mitra G (2004) Evidence for non-plane strain flattening along the Moine thrust, Loch Srath nan Aisinnin, northwest Scotland. J Struct Geol 26:1755–1772
Strine M, Wojtal S (2004) Evidence for non-plane strain flattening along the Moine thrust, Loch Strath nan Aisinnin, northwest Scotland. J Struct Geol 19:1755–1772
Tikoff B, Fossen H (1993) Simultaneous pure and simple shear: the unifying deformation matrix. Tectonophysics 217:267–283
Twiss RJ, Unruh JR (1998) Analysis of fault-slip inversions: Do they constrain stress or strain rate. J Geophys Res 103:12,205–12,222
White SH, Evans DJ, Zhong DL (1982) Fault rocks of the Moine thrust zone; microstructures and textures of selected mylonites. Textures Microstruct 5:33–61
Willet (1992) Dynamic and kinematic growth and change of a Coulomb wedge. In: McClay KR (ed) Thrust tectonics. Chapman and Hall, London, pp 19–31
Willet (1999) Orogeny and orography: The effects of erosion on the structure of mountain belts. J Geophys Res 104:28,957–28981